Novel Prediction Methods of Multicarrier Multipactor for Space Industry Standards

Sergio Anza, Jérôme Puech, David Raboso, Ulrich Wochner, Philippe Mader, Olivier Koch, Jean-Christophe Angevain, Un-Pyo Hong, Per Magnusson, Isabel Montero, Mohammed Belhaj, John Petit, Jordi Gil, Carlos Vicente, Vicente E. Boria, *Fellow, IEEE*

***Abstract*—Multipactor prediction methods are of high relevance for the space industry in order to prevent its appearance during the design phase of RF high power components. Up to the present time, prediction for multicarrier signals has been covered by an empirical rule, the 20-gap-crossing rule (20GCR), proposed in the 2003 version of the multipactor standard published by the European Cooperation for Space Standardization (ECSS). The 20GCR has been widely used by the space industry, although some studies have demonstrated that it might be inaccurate in some situations. The latest version of the ECSS multipactor standard, published in 2020, presents two novel methods for multipactor prediction with multicarrier signals: the pulsed method and the envelope sweep method, both simple, accurate enough and suitable for industry standards. Whereas the pulsed model is a simple and fast method based on a one-dimensional analytical theory, the envelope sweep method is more accurate and able to deal with real 3D microwave structures. This paper details both multipactor prediction methods, as well as their practical validation with a large dataset from previous analytical studies and experimental activities.**

***Index Terms*—High power, multicarrier signals, multipactor, passive circuits, RF signals, vacuum breakdown.**

I. Introduction

THE multipactor phenomenon, also known as multipactoring or multipaction, is an electronic discharge occurring in microwave devices operating at high power levels and vacuum condition [1]–[3]. The multipactor effect is caused by free electrons being accelerated inside the microwave device in synchronism with the RF fields. As a consequence, these electrons impact successively against the device walls with enough energy to release extra electrons, due to the Secondary Electron Emission (SEE) effect [4]. This produces an exponential increase of electrons until saturation or self conditioning of the surfaces is reached. A multipactor discharge produces signal noise, power reflection and, ultimately, the physical damage of the device.

Multipactor is, therefore, considered a dangerous effect in high-power vacuum applications and must be avoided at the design phase. This is especially true in the space industry sector, since the replacement of damaged RF components of in-orbit satellites is not possible. Therefore, multipactor prediction and test becomes crucial during the design phase of such systems and involved components.

The occurrence of multipactor depends on many parameters, such as the geometry of the device, the physical distribution and the strength of the electromagnetic fields, the RF signal characteristics, and the SEE properties of the materials. One important consideration about multipactor prediction is that the prediction uncertainty is strongly linked to the uncertainty on the Secondary Electron Yield (SEY) values of the materials. Material characterization is a rather complex physical problem, and thus, the current state of the art is not able to completely model the SEY of metal and dielectric surfaces, nor its change with time due to surface contamination (aging) [5]. This problem is more evident in dielectrics, where surface charging also plays an important role [6], [7]. Therefore, multipactor prediction aims at being conservative but precise enough, when compared to measurements, in order to avoid overdesign of the RF components.

During the last half century, several studies have been devoted to multipactor with single carrier signals and different geometries, such as parallel plates [3], [8], [9], coaxial [10], [11], rectangular [12], and circular waveguides [13], as well as with different materials including metals and dielectrics [6]. Numerical electromagnetic (EM) simulation codes have been developed as well, being able to model this RF breakdown phenomenon in complex 3D structures [14].

Multicarrier signals, understood as the addition of different Continuous Wave (CW) carriers, add time-varying dynamics to the electron motion, rendering the problem much more complex. New theories are able to analytically model multipactor under multicarrier signals, such as the nonstationary (NS) theory [15], or theories which approximate the electron population growth or absorption without directly solving the equations of motion [16], [17]. However, these theories are often rather intricate, which does not make them very suitable for their practical use by the industry sector.

The European Cooperation for Space Standardization (ECSS) publishes the Multipaction Design and Test standard [18], [19], covering all multipactor considerations during the

Sergio Anza, Jordi Gil and Carlos Vicente are with Dassault Systems/Simulia e-mail: (sergio.anza@3ds.com).

Jérôme Puech is with the Centre National d'Études Spatiales (CNES), France.

David Raboso and Jean-Christophe Angevain are with the European Space Agency (ESA), The Netherlands.

Ulrich Wochner is with TESAT Spacecom, Germany.

Philippe Mader is with Thales Alenia Space, France.

Olivier Koch is with OHB, Germany

Un-Pyo Hong is with Airbus, Germany.

Per Magnusson is with RUAG, Sweden.

Isabel Montero is with the Consejo Superior de Investigaciones Científicas (CSIC), Spain.

Mohammed Belhaj is with ONERA, France.

John Petit is with Valencia Space Consortium (VSC), Spain.

Vicente E. Boria are with Universitat Politècnica de Valencia (UPV), Spain.

design and test phases, in order to validate components as multipactor free. The ECSS standard published in 2003 uses the 20-gap-crossing rule (20GCR) as a prediction method for unmodulated multicarrier signals [18]. As part of the multipactor analysis, this rule has been widely used by the industry during the last years. However, it has been found that the 20GCR is an empirical method which lacks a physical basis, and that may be very conservative in many cases, and too optimistic in others [20]. Other standards, such as the one from the Aerospace Corporation one [21], do not cover the multicarrier case at all.

The latest 2020 version of the ECSS standard [19] presents two new methods for multipactor prediction with unmodulated multicarrier signals, as replacement to the cited 20GCR. These are the pulsed model (PM) and the envelope sweep (ES) approaches. They are aimed at overcoming the 20GCR shortcomings whilst maintaining simplicity.

The main objectives of this paper are to explain in detail these two novel multipactor prediction methods, and to confirm their validity. Section II introduces an important concept in multipactor with multicarrier signals, the worst-case phase condition. In Section III, the current prediction methods are briefly reviewed, including the 20GCR. Section IV gives equations and methodology for the two new prediction methods. Sections V, VI and VII compare the predicted threshold results with theoretical and experimental data, which have been gathered from different test campaigns. Finally, Section VIII presents the summary and conclusions of this work.

II. Worst-case phase condition

The result of combining a number K of CW unmodulated carriers, with amplitude V_i, frequency $\omega_i = 2\pi f_i$, and phase ϕ_i, for $i = 1, 2, ..., N$, is a time-varying envelope, $V_e(t)$ modulating a signal whose frequency oscillates in time around the mean frequency of all carriers, f_m.

$$V_e(t) = \sqrt{\left[\sum_{i=1}^{K} V_i \cos(\omega_i t + \phi_i)\right]^2 + \left[\sum_{i=1}^{K} V_i \sin(\omega_i t + \phi_i)\right]^2} \quad (1)$$

For a fixed configuration of carrier phases, the envelope is periodic with period T_e, and its shape depends on the relative phases of the carriers [15]. "On" intervals are defined as periods of the multicarrier envelope in which its amplitude is above the multipactor threshold and, therefore, there is electron production. "Off" intervals are those in which the amplitude of the multicarrier envelope is below the multipactor threshold, and there is electron absorption. If $V_e(t)$ varies slowly with respect to the mean frequency, i.e. $T_e >> 1/f_m$, this threshold corresponds to the single carrier multipactor threshold level of a CW signal of frequency f_m [16].

According to the long-term multipactor criterion for multicarrier signals [22], the condition for having a discharge is that the electron production during the "On" intervals is higher than the electron absorption during the "Off" intervals, in one period of the envelope.

Among all possible phase combinations, there will be a particular one which meets this criterion with the lowest amplitude of the RF EM field per carrier. This phase combination is called the "worst-case phase condition".

III. Current prediction methods

This section reviews the two current multipactor prediction methods for multicarrier signals. These are the empirical 20GCR [18], and phase global optimization, which employs analytical or numerical multipactor simulations.

A. The 20-gap-crossing rule

The 20GCR was established as an analytical multipactor prediction method in the 2003 ECSS standard [18]. This rule assumes two-surface, single-carrier multipactor conditions. Basically, the 20GCR establishes that under resonant conditions, a multipactor discharge will occur when electrons cross the gap between the two surfaces of the device, and impact with them, at least 20 consecutive times. Therefore, in order to develop a discharge, the multicarrier envelope needs to be above the single-carrier multipactor threshold for a minimum amount of time, T_{20}, which ensures 20 electron gap-crossings. The 20GCR is limited to parallel-plate or coaxial like geometries, where stable two-surface multipactor occurs. T_{20} has the following expression

$$T_{20} = 10\frac{n}{f} \quad (2)$$

where f is the lowest frequency of all carriers. The multipactor order n indicates the type of multipactor resonance for the single-carrier case, being the number of half-cycles of the RF fields that the electrons take to transit between plates [2]. The multipactor order can be analytically determined from the RF field frequency and amplitude, and the distance between plates. In (2) the maximum n is taken, which occurs at the single-carrier multipactor threshold.

The 20GCR only establishes T_{20}, but it does not specify how to find the multipactor threshold value. One possibility is to determine the phases and amplitudes of the multicarrier signal, by numerical optimization, to obtain an envelope "On" interval with a duration of $T_{on} = T_{20}$. Such an optimization is based solely on the envelope shape and it is computationally feasible. Another possibility, which avoids optimization, is to use analytical equations that provide boundary envelope values for different values of T_{on}, considering all phase combinations, such as Wolk's or Angevain's curves [23]. Fig. 1 shows an example of both methods for a 20-carrier multipactor signal.

The 20GCR is extremely simple but has some known drawbacks. First of all, it proposes a universal limit, 20 gap-crossings, without considering the SEY properties of the material nor the multicarrier signal characteristics. This number has been empirically obtained with a limited amount of data [24], and has no physical justification. Therefore, the 20GCR may produce large prediction errors, being extremely conservative most of the time, and in some situations even non-conservative [20]. On the other hand, the 20GCR is based on single-period events. This may result in overlooking potentially dangerous

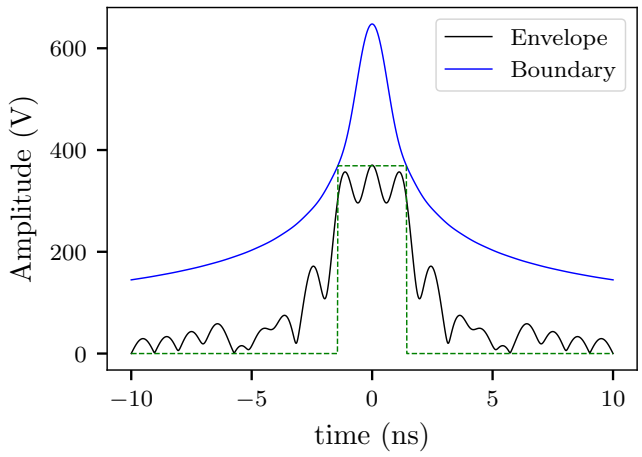

Fig. 1. Multicarrier envelope of a 20 carrier signal with mean frequency f_m = 11 GHz, frequency spacing Δf = 50 MHz. The period of the envelope is $T_e = 20$ ns. A 20GCR pulse of width $T_{20} = 2.85$ ns is plotted, corresponding to 2003 ECSS Silver coating [18], a gap $d = 0.45$ mm and a multipactor order of $n = 3$. Angevain's boundary function [23] is also included.

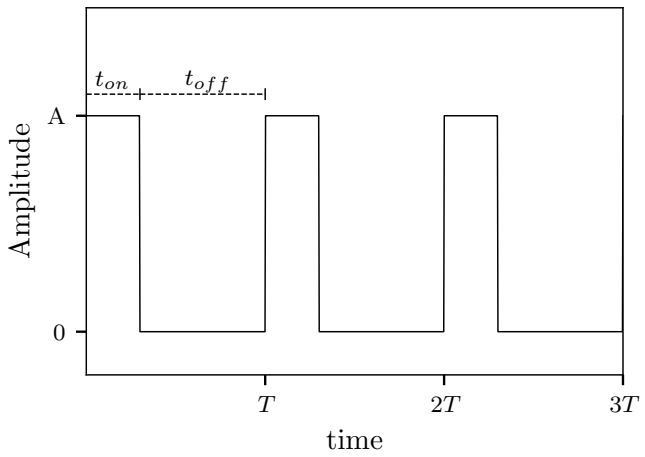

Fig. 2. PM definition. $t_{on} + t_{off} = T_e$

situations where the multicarrier envelope period is shorter than T_{20}, but the net sum of electrons generated during one envelope period is positive, leading to electron accumulation and maybe a long-term discharge [22]. There are other flavours of the 20GCR typically used in industry where the number of gap-crossings is modified, choosing for example 3GCR or 10 GCR, which may be more conservative but have the same inherent arbitrariness and limitations as the original 20GCR.

B. Global optimization

Global optimization consists of searching the worst-case phase combination within the phase-domain, in an efficient way, by minimizing the value of a cost function, while keeping the relative amplitudes among the carriers constant. In our case, the cost function is defined as the carrier amplitude leading to multipactor breakdown for each phase combination. This is, each phase combination leads to a different breakdown level, and the objective is to find the minimum one. There are different global optimization strategies available in the literature. Each one is suitable for different cost function properties. The main inconvenience of finding the worst case phase condition using a global optimizer is the vast number of phase combinations that must be checked.

Numerical tools, such as CST Studio Suite Fest3D/Spark3D™, are capable of performing full numerical simulations of multicarrier signals in 3D structures [25], [26]. However, the simulation time of a single phase combination is large enough to discourage the use of such an approach for the worst-case phase global optimization.

Some analytical multicarrier theories, such as the NS theory, are also able to perform a full multicarrier analysis for parallel-plate 1D geometries [15], [16]. These theories are less accurate and rather optimistic when applied to real 3D structures, since the parallel-plate 1D approximation is the worst-case for multipactor discharge in terms of geometry. However, being much faster than the 3D numerical counterpart, it is feasible to use them as an alternative to look for the "worst-case" solution by phase optimization. Furthermore, the theories themselves and the implementation of such tools are quite complex and time consuming to use in an industry standard.

IV. Novel Prediction Methods

Recently, the 2020 update of the ECSS Multipactor standard has introduced two novel prediction methods for multipactor and multicarrier signals [19]. The pulsed model, which approximates the multicarrier signal envelope to a rectangular pulse, and the envelope sweep, which looks for the worst-case phase combination in a reduced phase-space. The following sections provide a detailed description of both methods.

A. The Pulsed model

The pulsed model (PM) proposed in [19] is based on the long-term multipactor theory published in [22]. It is formulated for parallel-plate geometry, and it simplifies the multicarrier envelope to a rectangular pulse with constant amplitude V_{on}, above the single-carrier multipactor threshold, during the "On" interval, t_{on}, and 0 amplitude during the "Off" interval, t_{off} (see Fig. 2). During t_{on}, electrons are generated. During t_{off}, electrons are absorbed. The goal is to the determine V_{on} such that the electron absorption and generation compensate each other, producing a long-term multipactor discharge.

According to classical single-carrier theory [1], the electron generation during t_{on} is given by

$$\Gamma_{on} = \sigma_{on}^{\frac{2f_m}{n_{on}} t_{on}}, \tag{3}$$

where $\sigma_{on} \equiv \sigma(V_{on})$ and $n_{on} \equiv n(V_{on})$ are the SEY and multipactor order during resonance (depending on V_{on}) and f_m is the mean frequency of all carriers. Thus, for an initial number of electrons $N_0 \equiv N(t = 0)$, the number of electrons at the end of the "on" interval is $N(t_{on}) = N_0\Gamma_{on}$. Note that contrarily to the 20GCR, where the lowest frequency was taken, the PM takes the mean frequency as the reference one, since the average instantaneous frequency of a multicarrier

signal (equal amplitude for all carriers) is equal to the mean frequency of all carriers [15].

The electron absorption during t_{off}, Γ_{off}, can be obtained from the expression for the electron population, $N(t)$, given in [16]

$$\frac{dN}{dt} = N(\sigma(t) - 1)\frac{2f_m}{n(t)}, \tag{4}$$

where $\sigma(t)$ and $n(t)$ are SEY and order of impacting electrons in time, respectively. In turn, $n(t) = 2f_m\tau(t)$, where $\tau(t)$ is the electron transit time. Then, eq. 4 becomes

$$\frac{dN}{dt} = N\frac{\sigma(t) - 1}{\tau(t)}, \tag{5}$$

During the "Off" interval of the PM, the field amplitude is zero, thus the impact energy of the electrons is equal to their emission energy, which is in the order of few electron volts. Therefore, it is safe to assume that the SEY of impacting electrons during the "Off" interval is approximated by $\sigma(t) = \sigma_0$ which is a constant value of SEY for low energies that ranges from 0 to 1, depending on the material [22]. In addition, with a deterministic emission velocity of v_e, and in the absence of external electromagnetic field, the electron transit time is $\tau(t) = d/v_e$, where d is the gap distance. With this, the solution to the differential equation in Eq. 5 is given by

$$\Gamma_{off} = \exp\left(\frac{\sigma_0 - 1}{d/v_e}t_{off}\right) \tag{6}$$

which represents an exponential electron decay.

However, as shown in [16], the multipactor order for low or zero voltages is not constant but rather follows a quadratic increase. This is because the electron emission velocity is not a constant. The energy spectra of the emitted electrons depend on the energy of the impacting electrons and the surface composition. In a first approximation, we can assume that the emission velocity follows a probability density curve. More energetic electrons are absorbed first because low energy ones take longer to reach the opposite side. Hence, as time passes, the velocity distribution of the electrons between the two plates changes, moving to lower electron velocities, i.e the average velocity drops. Therefore, remaining electrons have an increased transit time. In [16], the electron transit time is approximated as $\tau(t) = d/v_e + \beta t^2$, where v_e is the average emission velocity and β a constant. Then, the solution of eq. 5 results

$$\Gamma_{off} = \exp\left(\frac{\pi}{2}\frac{\sigma_0 - 1}{d/v_e + \alpha t_{off}}t_{off}\right). \tag{7}$$

where $\alpha = \sqrt{\frac{d\beta}{v_e}}$, and the approximation $\arctan(x) \approx \frac{\pi}{2}\frac{x}{1+x}$ for $x \geq 0$ has been applied, in order to obtain a closed solution of the differential equation. The expression (7) is the one given in the ECSS Multipactor handbook [27].

The linear term αt_{off} produces a saturation of the absorption curve. Fig. 3 compares the exponential model, given by eq. 6, with the linear saturation model, given by eq. 7. In this figure, the normalized time is defined as tv_e/d. Exact electron absorption curves, computed with the NS theory [8], are included as a reference. Constant α has been set to $\alpha = 0.12(1 - \sigma_0)$, after performing a numerical fitting

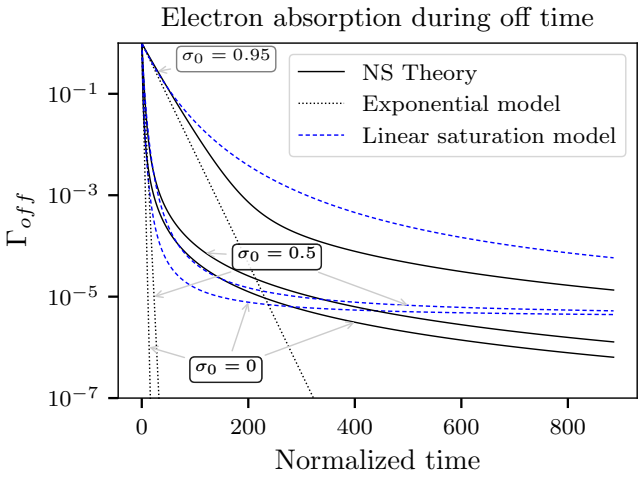

Fig. 3. Electron absorption curves for traditional exponential model, linear saturation model (7), and NS theory for different values of σ_0. The value of $\alpha = 0.12(1 - \sigma_0)$ has been numerically fitted.

taking the NS theory curves as a reference for the error calculation.This expression for α has been obtained for the whole range of possible σ_0 values, and therefore such an approximation can be generally used.

It can be observed that the linear saturation model, although not being very accurate, provides a better fitting to the real curve than the exponential model. For this reason, the former one is selected for the PM formulation.

Once the electron growth and absorption rates have been obtained, the number of electrons at the end of the period of the envelope is given by

$$N(T_e) = N_0\Gamma_{on}\Gamma_{off}, \tag{8}$$

where $N_0 \equiv N(t = 0)$ is the initial number of electrons. The long-term multipactor criterion states that the total electron production during an envelope period has to be equal to or greater than one, for multipactor to occur. Therefore from (8),

$$\frac{N(T_e)}{N_0} \geq 1 \rightarrow \Gamma_{on}\Gamma_{off} \geq 1. \tag{9}$$

Using (3) and (7) on (9), as well as the condition $t_{on} + t_{off} = T_e$, it is possible obtain that [27]

$$t_{on} = \frac{AB - C - \sqrt{(AB - C)^2 + 4AC\alpha T_e}}{2A\alpha}, \tag{10}$$

where

$$A = \frac{2f_m}{n_{on}}\log\sigma_{on} \tag{11}$$

$$B = \frac{d}{v_e} + \alpha T_e \tag{12}$$

$$C = \frac{\pi}{2}(\sigma_0 - 1) \tag{13}$$

Eq. (10) has a solution for values of $\sigma_{on} > 1$, with limits of $\lim_{\sigma\to\infty} t_{on} = 0$ and $\lim_{\sigma\to 1} t_{on} = T_e$.

Conceptually, the PM is similar to the 20GCR, but here, the length and amplitude of the pulse t_{on} and V_{on} are not fixed

values, but derived considering the surface SEY properties and signal characteristics. There are some obvious limitations in this simple approach. Approximating the multicarrier envelope by a square pulse of length t_{on} considers only phase combinations that maximize the signal energy in such an interval. Thus, only a subset of the solution domain is considered. On the other hand, although it is always possible to constrain the envelope to a rectangular shape (concentrating energy in an interval) by phase optimization, the resulting envelope does not have a constant amplitude, but presents ripples and sidelobes according to the number of carriers (see Fig. 1). The higher the number of carriers, the higher the resemblance of the multicarrier envelope to a rectangular pulse. In Sections V and VI it is shown that, despite these limitations, the PM predictions are more accurate than the 20GCR ones, and still remain conservative.

In eqs.(10 - 13) parameters f_m and T_e, are given as part of the signal characteristics. Parameter d corresponds to the gap size, given by the geometry of the device. In turn, σ_0 and v_e are specific to the coating material, whereas α is a fitting parameter obtained numerically. The only two unknown figures are σ_{on} and n_{on}, which are the SEY and multipactor order, respectively, corresponding to a single-carrier resonant discharge at amplitude V_{on}. In order to obtain them, any single-carrier theory or 1D numerical method can be used.

In this work , the main purpose is to provide simple methods suitable for industry standards, and therefore, we use simple approximations taken from the classical multipactor theory, which do also provide conservative results, one of the main concerns in multipactor prediction.

Firstly, the electrons depart from one plate with low energy and are accelerated towards the opposite one until they impact with velocity v_i. Therefore, it could be roughly approximated that the electrons travel from plate to plate with a constant velocity equal to $v_i/2$. Hence, the multipactor order n_{on} can be approximated as

$$n_{on} = \frac{4 f_m d}{v_i}. \tag{14}$$

In turn, the electron impact velocity can be approximated in two ways, depending on the multipactor order. For low multipactor orders, classical resonant multipactor equations of motion are valid, but for large multipactor orders, non-resonant multipactor equations should be used instead [28]. The impact velocity at V_{on} is approximated then as

$$v_i = 2v_\omega + v_e, \quad n_{th} < 3 \tag{15}$$

$$v_i = v_\omega + v_e + \frac{v_\omega^2}{2(v_\omega + v_e)}, \quad n_{th} \geq 3, \tag{16}$$

where

$$v_\omega = \frac{e}{m}\frac{V_{on}}{2\pi f_m d}, \tag{17}$$

and m and e are the electron mass and charge, respectively.

At multipactor threshold, the multipactor order is the term n_{th} used in (15) and (16). Also, the impact energy is equal to the first cross-over energy, W_1, for which the SEY is equal to 1. This figure is material dependent and must be given in the problem specifications. Therefore, impact velocity at threshold is $v_{th} = \sqrt{-\frac{2e}{m}W_1}$. Using (14) we obtain

$$n_{th} = \frac{4 f_m d}{v_{th}}. \tag{18}$$

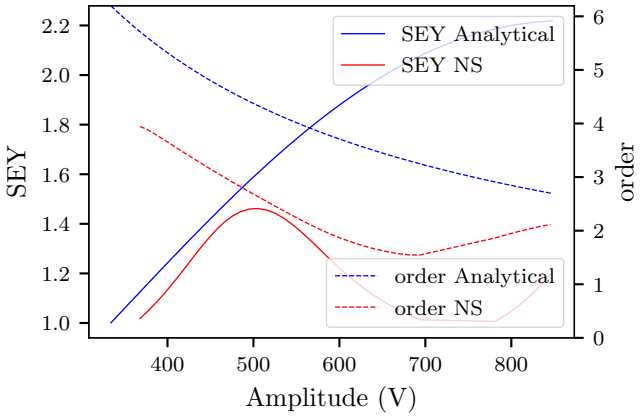

Fig. 4. Approximated SEY and order curves compared with NS theory computations for $f \times d = 5.04$ GHzmm and 2003 ECSS Silver coating [18].

Secondly, σ_{on} depends on the electron impact energy when V_{on} voltage is applied. The electron impact energy is obtained as $W_i = -\frac{m}{2e}v_i^2$. There are different analytical models that derive σ as a function of such impact energy. Here, the modified Vaughan model [29] is used.

Fig. 4 shows the SEY and order computed with (14)-(16), compared with NS theory for an $f \times d$ value of 5.04 GHzmm, and 2003 ECSS Silver coating [18]. The NS theory is considered the exact solution for 1D. In this example, the approximated SEY curve fits reasonably well the initial part of the NS theory one. But, right after the maximum SEY peak is reached, both curves diverge. Nevertheless, the initial part is the most important one for the multipactor threshold (SEY close to one), and therefore, the SEY approximation presented above is valid for our purposes. Regarding the multipactor order, the trend is similar to the NS theory curve, adding a constant error. This would imply a lower electron production rate as compared with the NS theory one. But, on the other hand, this error is partially compensated by the approximated SEY, which is larger than the NS counterpart. The results presented in Sections V and VI, indicate that the overall performance of the PM with this approach is satisfactory.

Thus, summarizing, the procedure would be the following for given f_m, d, and material W_1. The multipactor order at threshold n_{th} is computed using (18). Using the value that is determined, the electron impact velocity at V_{on}, v_i, is obtained from (15) to (17). Then, n_{on} is next computed using (14). Finally, σ_{on} is computed from the obtained value of v_i using the modified Vaughan formula [29].

Once σ_{on} and n_{on} have been determined, the V_{on} versus t_{on} curve can be derived. Fig. 5 (top), shows an example of such a curve.

In order to obtain the amplitude per carrier V_c (considering equal amplitudes), it is possible to either synthesize the mul-

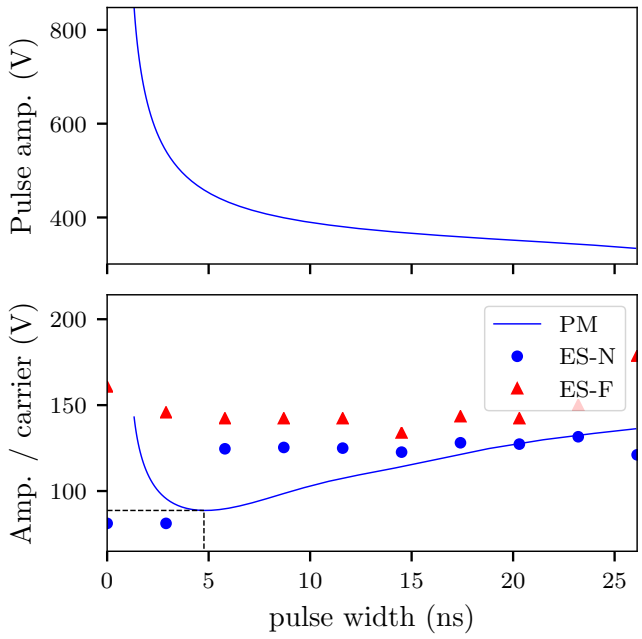

Fig. 5. PM curves obtained for $f \times d = 5.04$ GHzmm and 2003 ECSS Silver coating [18]. (top) pulse amplitude versus pulse width. (bottom) amplitude per carrier versus pulse width. ES results for the example of Section IV-C are included as well.ES-N and ES-F stand for simulations performed with NS theory and FEST3D™, respectively

ticarrier phases and amplitudes to obtain a pulse with t_{on} and V_{on} by optimization, or to use a boundary function $F_v(t_{on})$ such that

$$V_{on} = F_v(t_{on})V_c \tag{19}$$

In the example above the, the Angevain's modified sincsum curve [23] has been used with the expression

$$F_v(\tau) = \frac{\sqrt{\sum_{k=1}^{K} a_k^2 + 2\sum_{k=1}^{K-1}\sum_{i=k+1}^{K} a_k a_i \frac{\sin(\pi[f_k - f_i]\tau)}{\pi(f_k - f_i)\tau}}}{\frac{1}{K}\sum_{k=1}^{K} a_k} \tag{20}$$

where f_i and a_i are the frequency and amplitude, respectively, of the i-th carrier of the multicarrier signal, $i \in [1, K]$.

Fig. 5 (bottom) depicts the V_c versus t_{on} curve for the example being discussed. Note that there is a certain t_{on} for which V_c is minimum. This minimum value is selected as the multipactor threshold per carrier.

Finally in order to convert the value, V_c, from voltage to power, equivalent circuits or EM field analysis of the component are necessary. For instance, the electric field may be computed with a 3D software for 1W input power, at the mean frequency, and integrated along the gap line. This is called the "voltage at 1W", $V_{@1W}$. The input power P_i is then derived from

$$P_i = \left(\frac{V_c}{V_{@1W}}\right)^2 \tag{21}$$

B. The envelope sweep methodology

Finding the worst-case condition by phase optimization through the whole solution domain, as described in Section III-B, may imply a vast number of iterations. The aim of the envelope sweep (ES) approach is to drastically reduce the solution domain, in order to enable the use of 3D numerical software in reasonable computation times.

This domain reduction provides results close to the worst-case assuming that the breakdown voltage varies smoothly with the signal phases. This also assumes that, since different phase combinations may yield similar envelopes, there are multiple regions with values close to the lowest breakdown value [30]. See for example the breakdown voltage map of a four carrier multipactor signal in Fig. 6. It is seen that, apart from the global minimum, there are other large regions, with local minima, spread around the map, having similar values. This fact is more evident for larger $f \times d$ products (Fig. 6b). This means that selecting a phase combination different from the worst-case one, may not imply a big difference if it is located close to the worst-case one, or in a region with a local minimum.

Similarly to the PM, the ES approach of [19], considers the multicarrier signal envelope as a combination of two "On" and "Off" intervals. The method consists of sweeping the value of t_{on} with a certain number of points from $t_{on} = 0$ to $t_{on} = T_e$, and optimize, for each t_{on}, the carrier phases to match the envelope shape to the resulting rectangular pulse, of time duration T_{on}. The multipactor breakdown power is then analytically or numerically computed for each of the t_{on} values. Finally, the lowest breakdown power among all points is selected.

In this sense, the ES approach is similar to the PM since both methods use a rectangular pulse to reduce the solution domain, and both look for the t_{on} that provides the lowest breakdown level. The difference is that, whereas the latter uses single carrier theory to find an analytical approximation for the worst case, the former simulates a finite number of t_{on} values using full multi-carrier analysis, either analytically or numerically.

The ES methodology is open to particular implementations, following the same procedure [19]:

1) Select a certain number P of equi-spaced values for $t_{on,i} \quad i = 1, .., P$, ranging from $[0, T_e]$. The number of points should be high enough to ensure convergence.
2) Find the multicarrier signal phases for each of these points by constraining the envelope shape to a rectangular signal of duration $t_{on,i}$.
3) Perform a multipactor analysis with the phase values obtained for each point. The analysis must consider the real multicarrier signal with no simplifications. The analysis can be done by either 3D numerical software or employing full multicarrier theories. The output is the breakdown power for each of the selected points.
4) Choose the minimum breakdown power among all points.

Of course, this solution might not be the "worst-case phase condition" in a general case. This method assumes that differ-

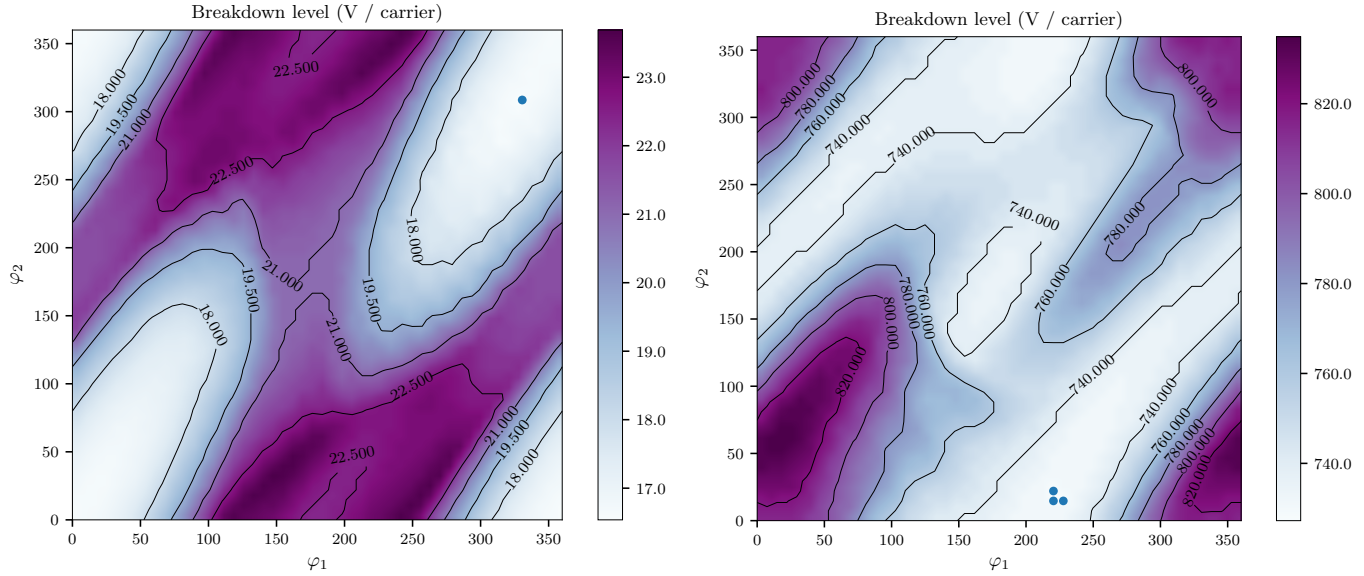

(a) $f \times d$ = 1 GHzmm (b) $f \times d$ = 20 GHzmm

Fig. 6. Breakdown level map for each carrier phase combination (only 2 degrees of freedom) computed with NS theory. For all cases the multicarrier signal has 4 carriers with an mean frequency of 11 GHz and a frequency spacing of Δf = 100 MHz. Coating material is 2003 ECSS Silver of Table II. Minima are marked with blue dots.

ent phase combinations, yielding envelopes with the power concentrated in intervals of similar size, will have similar breakdown power. Therefore, since it covers the complete range of possible interval sizes, the solution is expected to be close to the optimum one.

This work presents a specific implementation of the ES methodology. The t_{on} range has been divided into 10 equally-spaced points from 0 to T_e. The multicarrier envelope has been matched to each pulse width using a genetic global optimizer [31]. The envelope amplitude is constrained to be equal or higher than the pulse amplitude during the pulse length, with minimum amplitude per carrier. In step 3, the multipactor analysis has been done with NS 1D parallel-plate theory [15] (ES-N), as well as with numerical simulations with CST Studio Suite Fest3D™ software, from now on Fest3D™ (labeled as ES-F).

C. Practical Example

In this section, a practical example is used to demonstrate the prediction methods presented. It consists of a corrugated Ku-band transformer in waveguide technology, with WR75 interface and critical gap size of $d = 0.42$ mm. Experimental data for multipactor breakdown power are available for both single and multi-carrier signals in [20]. The experimental breakdown power is 201 W per carrier. The multicarrier signal has 6 carriers with frequencies described in Table I. The device is Silver coated, therefore, SEY parameters of the 2003 ECSS silver [18] have been taken as shown in Table II. Version of 2003 has been chosen instead of the new 2020 update, since more multipactor prediction data are available in literature, and they are used by the 20GCR and by the Multipactor Tool, thus enabling a direct comparison. A secondary electron release energy of 1.5 eV has been assumed for all 1D analytical

TABLE I
SAMPLE PARAMETERS FOR WR75 TRANSFORMER OF [20].

Carriers	f_m (GHz)	Δf (MHz)	d (mm)	V_{1W} (V)	$f \times d$ (GHzmm)	n
6	11.992	38.3	0.42	8.9	5.03	3

TABLE II
SEY FIGURES FOR 2003 ECSS SILVER AND ALUMINIUM OF [18]

	W_1 (eV)	W_{max} (eV)	σ_{max}	σ_0
ECSS Silver	30	165	2.23	0.5
ECSS Aluminium	23	150	2.98	0.5

methods. Numerical 3D simulations use an electron emission of 3 eV, doubling the 1D case because the electrons are released with non-zero angle close to 45^o [32]. In order to make the voltage to power conversion, eq. (21) is used. The voltage at 1W is computed with Fest3D™ 3D fields integrated along the gap line, resulting in $V_{1W} = 8.9$ V.

The PM procedure of Section IV-A has been followed. The ES method has been implemented as per Section IV-B. Fig. 7 shows the phase conformance results to different pulse widths for this particular example. For each phase configuration, two types of simulation have been done: 3D numerical simulation with Fest3D™ software tool, and parallel-plate NS analytical analysis. Fig. 5 shows the Voltage versus t_{on} curve for this example. On top, the solution to eq. (10) is shown. At bottom, the voltage per carrier can be seen, after applying (20) to (10). Results for PM show a minimum at 5 ns with a value of 88.7 V. Results for ES method with NS theory (ES-N) and Fest3D™ simulations (ES-F) follow the same trend, with the exception

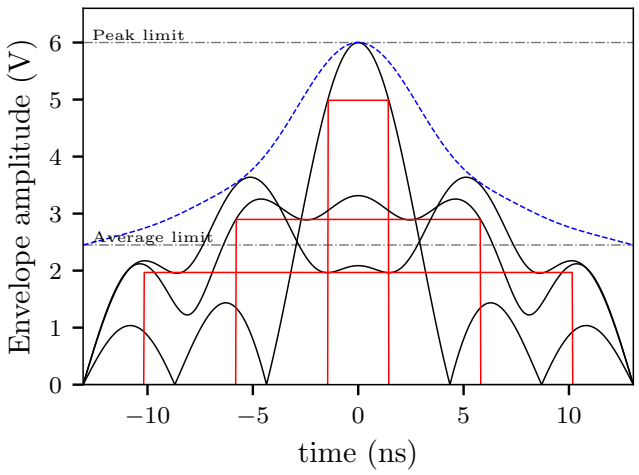

Fig. 7. Multipactor phase conformance for different pulse widths in the ES procedure of the WR75 transformer example. Only three pulse widths have been plotted, corresponding to the points $t_{on,2} = 2.9$ ns, $t_{on,5} = 11.6$ ns, $t_{on,8} = 20.3$ ns

TABLE III
BREAKDOWN POWER LEVELS FOR WR75 TRANSFORMER EXAMPLE.

Result	Voltage (V)	Power (W)	Error (dB)
Experimental	125.6	201	—
PM	88.7	99.8	3
ES-N	81.2	83.6	3.8
ES-F	133.4	227	-0.5
20G	60	45.4	6.5
20GB	54.5	37.6	7.3

of the first points. The reason behind is due to the fact that simulations with Fest3D™ consider a real structure, where the field distribution is not homogeneous. Therefore, for low pulse widths, the "Off" time is large, and electrons tend to be pushed outside from the high field regions, due to the ponderomotive force [12]. This effect is neither considered in the PM nor in the 1D NS theory, and it is the reason for the discrepancy in such points.

The predicted breakdown levels of PM and ES methods are summarized in Table III. There, 20GCR predictions are also included for comparison, in two different cases, the 20GCR with phase optimization (labeled as 20G) and with boundary curve (labeled as 20GB). The 20GCR methods present a larger error than the PM and ES ones. Specifically, the most accurate is the ES-F one (ES with Fest3D™ numerical simulations), since Fest3D™ considers the real 3D structure and EM field distribution. Although the error is negative, a value of -0.5 dB is very low and within the range of typical accuracy of experimental test beds.

V. ANALYTICAL VERIFICATION

The prediction methods described in Section IV have been tested with a large number of parallel-plate cases employing only analytical/numerical data.

The compared prediction methods are the PM and ES approaches. The ES approach is analyzed through the non-stationary theory (ES-N) and the Fest3D™ numerical solver simulations (ES-F). The 20GCR with phase optimization (20G) and with boundary curve (20GB), have been implemented as established in the ECSS standard 2003 version and using the Multipactor Tool [33] software utility. Global phase optimization has been done with NS multipactor theory (GNS) [15], using the optimization procedure of [30].

For the ES-F method, coaxial lines with an inner conductor of a fixed 12 mm radius have been employed, varying the outer conductor radius to obtain the different gap distances. A coaxial line has been selected, instead of a rectangular waveguide, for two reasons. First, coaxial lines behave like parallel-plate geometry when the ratio between outer and inner radius is near unity. And second, because in coaxial lines, despite the EM fields not being homogeneous along the gap, there are no low EM field regions within the structure. Hence, during the "Off" intervals, electrons remain in high field areas and are not lost. Therefore, for multicarrier signals, coaxial structures yield results closer to infinite parallel-plate geometry than rectangular waveguide ones.

GNS method has been selected as the reference for the error computation, since this method considers the whole solution space and theoretically finds the "worst-case phase condition". It is interesting to study this error, because the GNS method can be considered as the ideal 1D parallel-plate prediction. Comparing the proposed methods to the GNS one, provides information about their accuracy, without the uncertainties present in the tests, such as SEY variation due to aging, mechanical tolerances, thermal considerations or measurement errors.

Two different SEY curves have been considered, those for ECSS Silver and ECSS Aluminium with the parameters given by the ECSS standard of 2003 and summarized in Table II. Version of 2003 has been chosen for the same reasons stated in previous sections: there is more data available in the literature and allows a direct comparison with Multipactor Tool 20GCR results. Nevertheless, these methods are valid for arbitrary SEY curves.

Different parameters have been tested, such as the number of carriers, the frequency band, the frequency spacing between adjacent carriers, and the critical gap distance.. Table IV and Table V (see Appendix A) show the results for ECSS Silver and Aluminium, respectively. The prediction error of each method in dB, with respect to the GNS one, is summarized in Fig. 8. Positive error stands for a conservative error. It can be observed, in first place, that ES-N and ES-F methods have an error close to zero, with the exception of a single point for ES-F which has a -4 dB error. It should be remembered that this error is with respect to 1D parallel plate ideal result, and ES-F is considering 3D real structures, and the number of electrons as a whole number (analytical methods may deal with particles of fractional charge). The error of -4 dB corresponds to row 3 of Table IV, which has a very short gap (0.09 mm) and low $\Delta f = 50MHz$. This implies large t_{off} times. For 1D analytical NS theory, at the end of the "Off" intervals the number of electrons is usually below one, but during the next

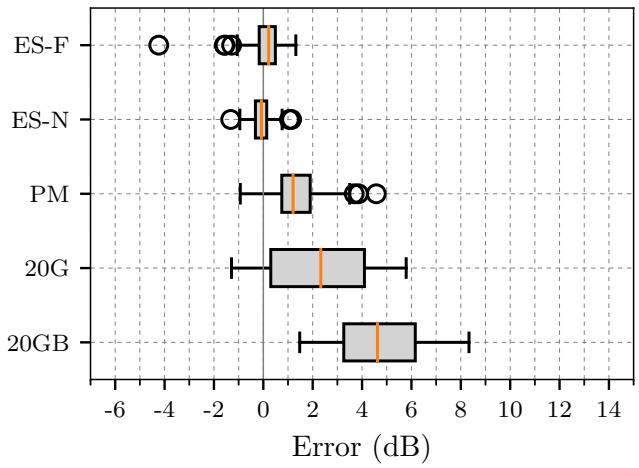

Fig. 8. Error bar plot of the multipactor predicted levels for the analytical dataset. It is computed with respect to the global NS analytical method (GNS). Positive error corresponds to a conservative prediction. Orange lines indicate the error median.Boxes extend from the lower to upper quartile values of the data. Lines cover 1.5 times the inter-fourth range from the median. Circles denote outliers points outside the line extremes.

"On" interval it may increase again, producing a discharge. For numerical simulations, in which the number of electrons is an integer number, it is very likely that, if the number of electrons reaches one, the last electron gets absorbed before the "On" interval starts. This is the reason why, when comparing the ES-F prediction results with those of GNS, there is such a high negative error. However, ES-F results are probably closer to reality.

On the other hand, the PM results show an error around 1 dB, lower than the error of the 20G and 20GB, which is around 2 dB and 5 dB respectively. 20GB method even has a case with more than 13 dB positive margin. Overall, according to the analytical verification, the ES method is the most accurate, followed by PM. 20GCR methods have larger errors (and are more conservative).

VI. Experimental verification

Experimental verification has been done with results of three different multipactor test campaigns with multicarrier signals.

A. ESA funded activity 1

This activity consisted in the design and the manufacturing of rectangular waveguide devices of different gaps in C-band and Ku-band frequencies, in order to obtain measurement data for different $f \times d$ ranges. Multicarrier signals of 6 and 8 carriers were used, with different frequency spacing between adjacent carriers. Different kinds of components were tested, such as transformers (TF), corrugated low-pass filters (LP) and bandpass filters (BP). More accurate description of the samples, signals, test bed and results can be found in [16], [20]. Table VI in the Appendix A shows the prediction and test results. ECSS 2003 Silver SEY of Table II has been used.

Notice that there are many samples for which there are no test results. This is because in many cases the breakdown power was beyond the available power delivered by the test bed. This implies that there are not much data for large gaps.

B. ESA funded activity 2

This activity included the design and manufacturing of three X-band samples. Tests were conducted with up to 10 carriers with frequency spacing of multiples of 99 MHz. Details of the activity can be found in [34].

Table VII in the Appendix A shows the prediction and test results. In this case, ECSS 2003 Silver of Table II was used for all prediction methods.

The empty fields in the measurement column correspond to untested cases, but they are included in the table since they provide prediction values which may be valuable for future comparison.

C. CNES and Thales Alenia Space activity

This activity was conducted under Centre National des Etudes Spatiales (CNES) R&T program R-S13/TC-0007-062 with Thales Alenia Space France as contractor. The main goal of the test bench was to determine the Multipactor threshold in multi-carrier operation. Two simple impedance transformers were manufactured with two different gaps, of values 0.2 mm and 0.3 mm, respectively. Only two carriers were used, but the frequency spacing was varied to obtain different envelope periods. The carriers have a mean frequency around 4 GHz. This implies a $f \times d$ of 0.8 GHzmm and 1.2 GHz mm, respectively, corresponding both to a nominal multipactor order of 1. According to the 20GCR, for very short envelope periods, shorter than $T_{20} = 2.5$ ns, no breakdown is possible.

To avoid any phases uncertainties (i.e. stable ratio between power above threshold and power below), the idea consisted in using a two carriers signal configuration. As far as the signal generation is concerned, a diplexer was inserted in the RF circuit to combine the 2 frequencies after the amplification. Moreover, the pulsed mode was selected in order to prevent any thermal issues. The standard detection methods were also used: phase nulling, third harmonic and return loss. As for seeding, a radioactive source and an electron gun were both installed in the vacuum chamber to be operated simultaneously and to guarantee a good reproducibility level of the measurements.

For the test procedure, a protocol was set up in the frame of this study. For a given frequency configuration that is to say for given frequencies of the 2 signals, the power per carrier was increased simultaneously until the threshold was reached. The spectral configuration being identical, the threshold between simulations and measurements can thus be compared. Moreover, the time needed for the instantaneous power to be above the single-carrier threshold and the needed time ratio for the Multipactor to appear can be estimated thanks to the configuration of the test bench. Here, time ratio stands as the time corresponding to the instantaneous power above the single-carrier threshold over the time corresponding to the instantaneous power below this same threshold.

VII. Summary of Results

For ESA activities of Sections VI-A and VI-B, the error of all prediction methods has been computed with respect to the experimental breakdown. Fig. 9 shows the statistics of such errors.

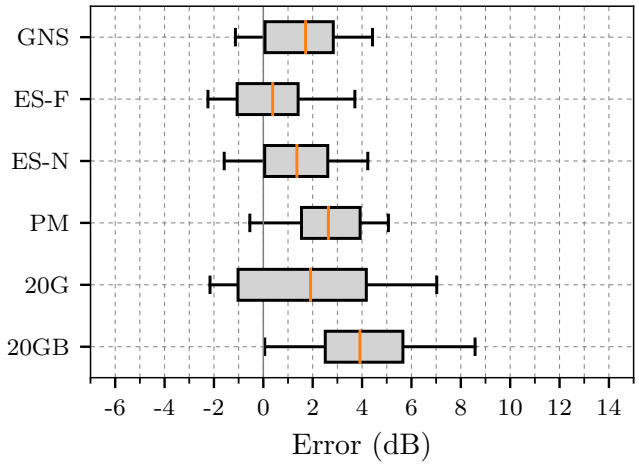

Fig. 9. Error bar plot of the predicted levels compared to experimental results for ESA activities of Sections VI-A and VI-B. Positive error corresponds to a conservative prediction. Orange lines indicate the error median.Boxes extend from the lower to upper quartile values of the data. Lines cover 1.5 times the inter-fourth range from the median.

Similarly to the analytical verification of Section V, ES methods, specially the ES-F one, are the most accurate. In this case, the PM, GNS, 20G and 20GB methods are quite similar, with errors around 3 dB, 2 dB, 3 dB and 4 dB, respectively. However, the spread of the error in the 20G methods is considerably larger than in the others, which brings out that the 20GCR might be either excessively conservative, for low multipactor orders, or even non conservative, for large multipactor orders [20].

In the case of the CNES and Thales Alenia Space activity of Section VI-C, predictions have been computed using the ECSS 2003 aluminium SEY parameters of Table II.

Table VIII in Appendix A presents the results for both samples. Fig. 10 shows the same results in a graphical way. The error is computed against measurements. In both samples, all methods follow a similar trend for low frequency spacing, 20GCR methods being significantly more conservative. However, for larger spacings 20GCR methods tend to have a larger negative error. In fact, for the last point, $\Delta f = 800$ MHz, none of the 20GCR methods predict a breakdown, since the envelope period, $T_e = 1.25$ ns, is shorter than $T_{20} = 2.5$ ns. However, tests produced a discharge for such a value of Δf. The most important conclusion of this experiment is that the 20GCR may overstimate, or completely neglect the multipactor breakdown for some cases.

VIII. Conclusion

This work presents two novel multipactor prediction methods with unmodulated multicarrier signals. These two methods, called Pulsed Model and Envelope Sweep, have been

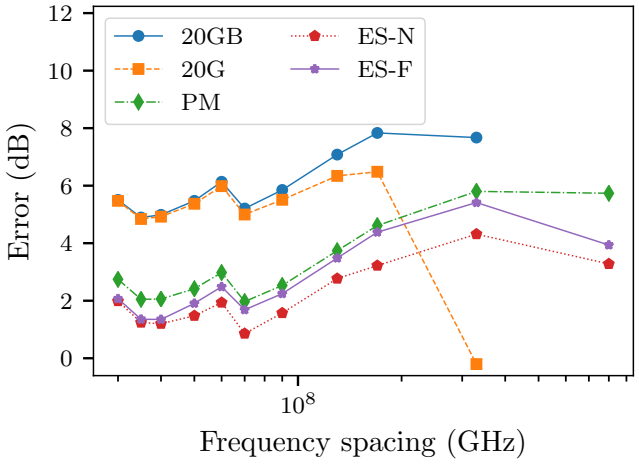

(a) 0.2mm gap

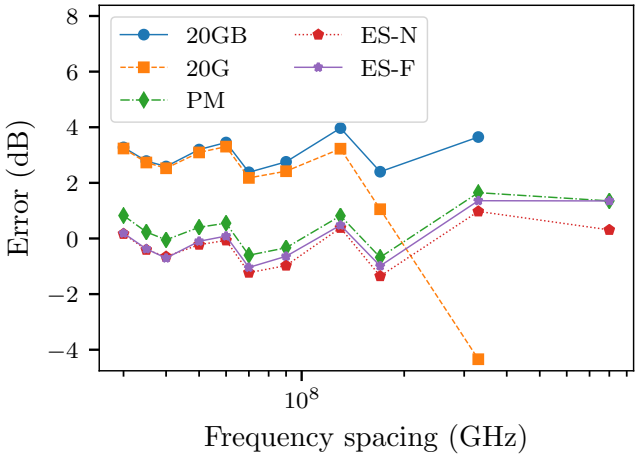

(b) 0.3mm gap

Fig. 10. Error in dB of the predicted multipactor breakdown levels compared to experimental results for CNES and Thales Alenia Space activity. Positive error corresponds to conservative prediction.

developed for the end user and are described in the new ECSS multipactor standard issued in 2020 [19]. They are intended to be easily implemented by RF engineers, and accurate enough to be reliable for multipactor prediction in industry standards.

The comparison of these two new methods, with the 20GCR of the previous 2003 ECSS standard [18], reveals that the newest improve on the previous one in terms of accuracy and reliability. Therefore, this justifies the substitution of the 20GCR by any of these two new methods. Test results have also shown an important aspect of the 20GCR that was also highlighted in previous publications: it may be not conservative in some specific cases. In fact, for the two carrier campaign of CNES and Thales Alenia Space activity (Section VI-C), the 20GCR was not predicting any discharge at all for the maximum frequency spacing, whereas ES and PM predictions, together with experimental results showed otherwise.

Regarding the two new methods, the PM method provides analytically fast predictions, with parallel-plate geometries.

This fast analysis is important in the design phase, although it gives more conservative results than the ES method. In turn, the ES method reduces the solution domain enabling the use of 3D numerical software and full signal analysis at a reasonable computational cost. This was not possible with previous methods, and enables the accurate study of complex 3D structures with multicarrier signals.

This work appends a large analytical, numerical and experimental dataset of multipactor breakdown with multicarrier signals, for many different combinations of numbers of carriers, frequencies and gaps, gathered from different test activities. They will be very useful as a reference for future work in this field.

APPENDIX A
PREDICTION AND TEST RESULTS DATA

Prediction and test results of Sections V and VI are presented here in tabulated form. In the next tables, $V1W$ is the $V@1W$ used in eq. 21, whereas the labels 20G, 20GB, PM, ES-N, ES-F and GNS indicate the threshold given by the different prediction methods as detailed in sections IV-A and IV-B. On the other hand, MEAS column contains the multipactor power threshold obtained in experimental results (the lowest measured value for each sample).

TABLE IV
PREDICTED BREAKDOWN VOLTAGES FOR THE ANALYTICAL VERIFICATION SET WITH ECSS SILVER.

K	f_m (GHz)	Δf (MHz)	d (mm)	V_{1W} (V)	20G (V)	20GB (V)	PM (V)	ES-N (V)	ES-F (V)	GNS (V)
4	11	50	0.09	0.95	9.9	9.8	13.7	14.6	17.5	14.6
4	11	100	0.09	0.95	10.3	9.9	15	16.6	16	16.6
10	11	50	0.09	0.95	4.3	4	6.4	7.3	11.8	7.3
10	11	100	0.09	0.95	5.8	4.4	7.5	11.1	10.7	10.6
20	11	50	0.09	0.95	2.9	2.2	3.9	6.2	6.8	5.7
20	11	100	0.09	0.95	4.4	2.9	4.8	7.2	6.8	7.1
4	4	50	0.25	1.57	10.8	10.1	15.8	17.9	17.1	17.9
4	4	100	0.25	1.57	15.5	11.1	17.4	22.9	21	22.9
10	4	50	0.25	1.57	7.2	4.8	8.2	11.3	11.5	11.5
10	4	100	0.25	1.57	8.3	6.8	9.7	13.8	12.9	14.8
20	4	50	0.25	1.57	4.5	3.4	5.4	8.4	8	8.4
20	4	100	0.25	1.57	7.2	5.1	6.7	10	9.8	11.3
4	11	50	0.45	2.1	86.6	79.8	123	115	119	115
4	11	100	0.45	2.1	130	88.4	134	166	165	142
10	11	50	0.45	2.1	57.1	38.2	66.6	80.1	85	77.6
10	11	100	0.45	2.1	63.3	52	77.3	84.2	86.9	85.6
20	11	50	0.45	2.1	36.3	26	45.7	47.8	53.3	54.6
20	11	100	0.45	2.1	48	35.1	53.4	61.2	62.3	63.4
4	4	50	1.25	3.45	176	99.4	139	170	170	155
4	4	100	1.25	3.45	172	135	146	171	170	159
10	4	50	1.25	3.45	70.6	60.1	82.6	93	95.7	89.7
10	4	100	1.25	3.45	98.7	81	88.9	103	105	102
20	4	50	1.25	3.45	53.7	40.6	57	64.4	66	70.3
20	4	100	1.25	3.45	81.7	52.8	61.6	79.3	76.4	74.9
4	11	50	0.9	2.95	329	186	267	298	303	298
4	11	100	0.9	2.95	356	255	283	359	347	348
10	11	50	0.9	2.95	142	112	155	200	199	195
10	11	100	0.9	2.95	187	155	172	213	218	210
20	11	50	0.9	2.95	97.4	77.6	107	133	134	142
20	11	100	0.9	2.95	129	90	119	145	151	149
4	4	50	2.5	4.79	373	291	291	365	350	358
4	4	100	2.5	4.79	372	301	299	366	353	366
10	4	50	2.5	4.79	221	180	178	222	223	220
10	4	100	2.5	4.79	231	174	184	228	223	229
20	4	50	2.5	4.79	147	104	123	151	153	159
20	4	100	2.5	4.79	164	106	128	161	157	150
4	11	50	1.8	4.09	711	494	566	720	699	707
4	11	100	1.8	4.09	785	600	585	731	699	731
10	11	50	1.8	4.09	383	302	344	425	431	431
10	11	100	1.8	4.09	491	374	359	456	439	446
20	11	50	1.8	4.09	310	210	237	295	296	314
20	11	100	1.8	4.09	363	250	249	313	313	313
4	4	50	5	6.47	820	613	597	742	720	738
4	4	100	5	6.47	741	558	606	760	720	760
10	4	50	5	6.47	478	364	367	462	455	463
10	4	100	5	6.47	421	340	373	453	446	432
20	4	50	5	6.47	337	239	256	321	322	306
20	4	100	5	6.47	309	203	261	318	309	295

ACKNOWLEDGMENT

The authors would like to thank the ESA-ESTEC and ASD-Eurospace for the creation and support of the ECSS-E-ST-20-01 working group, for the update of the ECSS multipactor standard, which has been the motivation of this work.

REFERENCES

[1] E. W. B. Gill and A. von Engel, "Starting potentials of high-frequency gas discharges at low pressure," *Proceedings of the Royal Society of London, Series A, Mathematical and Physical Sciences*, vol. 192, no. 1030, pp. 446–463, Feb. 1948.

[2] A. Hatch and H. Williams, "The secondary electron resonance mechanism of low-pressure high-frequency gas breakdown," *Journal of Applied Physics*, vol. 25, no. 4, pp. 417–423, Apr. 1954.

[3] J. R. M. Vaughan, "Multipactor," *IEEE Trans. Electron Devices*, vol. 35, pp. 1172–1180, Jul. 1988.

[4] ——, "A new formula for secondary emission yield," *IEEE Transactions on Electron Devices*, vol. 36, no. 9, pp. 1963–1967, 1989.

[5] E. Sorolla, M. Belhaj, J. Sombrin, and J. Puech, "New multipactor dynamics in presence of dielectrics," *Physics of Plasmas*, vol. 24, no. 10, p. 103508, 2017. [Online]. Available: https://doi.org/10.1063/1.5001832

[6] J. Vague, J. C. Melgarejo, M. Guglielmi, V. E. Boria, S. Anza, C. Vicente, M. R. Moreno, M. Taroncher, B. Gimeno Martínez, and D. Raboso, "Multipactor effect characterization of dielectric materials for space applications," *IEEE Transactions on Microwave Theory and Techniques*, vol. 66, no. 8, pp. 3644–3655, Aug 2018.

[7] L. Olano and I. Montero, "Energy spectra of secondary electrons in dielectric materials by charging analysis," *Results in Physics*, vol. 19, p. 103456, 2020.

[8] S. Anza, C. Vicente, J. Gil, V. E. Boria, B. Gimeno, and D. Raboso, "Nonstationary statistical theory for multipactor," *Physics of Plasmas*, vol. 17, no. 6, p. 062110, June 2010.

[9] M. Siddiqi and R. A. Kishek, "A predictive model for two-surface multipactor stability and growth based on chaos theory," *Physics of Plasmas*, vol. 26, no. 4, p. 043104, 2019. [Online]. Available: https://doi.org/10.1063/1.5087586

[10] D. Gonzalez-Iglesias, A. M. Perez, S. Anza, J. Vague, B. Gimeno, V. E. Boria, D. Raboso, C. Vicente, J. Gil, F. Caspers, and L. Conde, "Multipactor in a coaxial line under the presence of an axial dc magnetic field," *Electron Device Letters, IEEE*, vol. PP, no. 99, pp. 1 –3, 2012.

TABLE V
PREDICTED BREAKDOWN VOLTAGES FOR THE ANALYTICAL VERIFICATION SET WITH ECSS ALUMINIUM

K	f_m (GHz)	Δf (MHz)	d (mm)	V_{1W} (V)	20G (V)	20GB (V)	PM (V)	ES-N (V)	ES-F (V)	GNS (V)
4	11	50	0.09	0.95	6.8	6.8	11.5	11.6	11.2	11.5
4	11	100	0.09	0.95	7.1	6.9	12.6	12.7	11.8	12.7
10	11	50	0.09	0.95	3	2.8	5.4	5.4	5.5	5.4
10	11	100	0.09	0.95	4	3	6.2	6.6	6	6.6
20	11	50	0.09	0.95	2	1.5	3.2	3.4	3.6	3.5
20	11	100	0.09	0.95	2.9	2	3.9	5.4	4.9	5.2
4	4	50	0.25	1.57	7.5	7	13.3	13.6	12.4	13.6
4	4	100	0.25	1.57	10.7	7.7	14.6	15.8	13.6	15.8
10	4	50	0.25	1.57	5	3.3	6.8	7.6	8.5	7.6
10	4	100	0.25	1.57	5.7	4.7	8	10.1	9.3	10.6
20	4	50	0.25	1.57	3.5	2.4	4.4	6	5.2	5.9
20	4	100	0.25	1.57	4.5	3.5	5.5	7.7	6.8	7.8
4	11	50	0.45	2.1	55.9	51.6	104	98.8	93.5	98.8
4	11	100	0.45	2.1	84.1	57.1	113	108	107	108
10	11	50	0.45	2.1	36.9	24.6	55.7	50	51.2	50
10	11	100	0.45	2.1	40.9	33.6	64.2	74.5	71.6	69.6
20	11	50	0.45	2.1	23.7	16.8	37.6	39.3	39.1	40.5
20	11	100	0.45	2.1	32.1	22.7	44.3	45.6	44.1	48.4
4	4	50	1.25	3.45	114	64.2	117	114	113	114
4	4	100	1.25	3.45	111	86	123	122	124	122
10	4	50	1.25	3.45	46.7	39.2	68.5	77.9	74.9	72.6
10	4	100	1.25	3.45	63.7	52.4	74.5	76.4	75.4	77.6
20	4	50	1.25	3.45	36	26.2	47.3	50.8	48.6	52.1
20	4	100	1.25	3.45	47.9	34.2	51.4	55.9	53.7	57.6
4	11	50	0.9	2.95	141	110	226	235	222	235
4	11	100	0.9	2.95	225	139	239	257	252	257
10	11	50	0.9	2.95	78.1	62.5	128	158	147	151
10	11	100	0.9	2.95	103	84.9	142	168	158	161
20	11	50	0.9	2.95	57.3	42.5	88.7	100	95.3	102
20	11	100	0.9	2.95	85	58	98.3	112	108	114
4	4	50	2.5	4.79	227	163	246	270	264	270
4	4	100	2.5	4.79	270	191	252	286	266	286
10	4	50	2.5	4.79	120	98.9	149	174	163	167
10	4	100	2.5	4.79	150	112	154	180	167	177
20	4	50	2.5	4.79	88	67.2	103	117	114	119
20	4	100	2.5	4.79	104	68.2	107	122	114	117
4	11	50	1.8	4.09	454	292	477	532	503	532
4	11	100	1.8	4.09	519	386	494	583	523	562
10	11	50	1.8	4.09	233	179	285	335	315	324
10	11	100	1.8	4.09	315	240	301	341	331	345
20	11	50	1.8	4.09	179	124	197	227	212	239
20	11	100	1.8	4.09	236	154	208	239	230	241
4	4	50	5	6.47	571	391	504	595	539	592
4	4	100	5	6.47	478	387	511	608	544	602
10	4	50	5	6.47	313	234	308	366	338	362
10	4	100	5	6.47	256	213	313	363	338	334
20	4	50	5	6.47	227	155	214	247	237	240
20	4	100	5	6.47	190	132	218	251	230	225

TABLE VI
PREDICTED BREAKDOWN POWERS FOR THE EXPERIMENTAL VERIFICATION SET OF ESA ACTIVITY 1.

Typ.	K	f_m (GHz)	Δf (MHz)	d (mm)	V (W)	20G (W)	20GB (W)	PM (W)	ES-N (W)	ES-F (W)	GNS (W)	MEAS (W)
LP	6	3.82	100	0.43	5.16	33.4	16.3	21.2	25.3	27.9	25.1	22.3
TF	6	3.82	100	0.43	4.03	54.8	26.7	34.8	41.4	46.4	41.2	40.9
LP	8	3.82	100	0.43	5.16	17.7	11.2	15.2	19.8	31.4	18.6	20.8
TF	8	3.82	100	0.43	4.03	29	18.4	25	32.5	50.4	30.5	45.3
LP	6	3.82	100	1.3	9.76	227	125	140	180	202	169	138
LP	8	3.82	100	1.3	9.76	128	91.1	105	133	155	120	92.3
LP	6	12	38.3	0.14	6.35	7.7	7.5	7.1	9.9	13.2	9.9	—
TF	6	12	38.3	0.14	3.89	20.4	20	18.9	26.5	34.1	26.3	58.6
LP	8	12	38.3	0.14	6.35	4.4	4.2	4.5	5.9	8.3	5.9	—
TF	8	12	38.3	0.14	3.89	11.7	11.3	11.9	15.7	20.1	15.7	30
LP	6	12	76.6	0.14	6.35	8.3	7.6	9	11.1	15.2	11.1	—
TF	6	12	76.6	0.14	3.89	22.1	20.4	24	29.6	35.2	29.6	48.5
LP	8	12	76.6	0.14	6.35	5.1	4.4	5.9	6.7	10.1	6.7	—
TF	8	12	76.6	0.14	3.89	13.6	11.7	15.8	17.7	20.9	17.7	29
LP	6	12	38.3	0.42	9.14	42.8	35.5	94.2	78.9	215	78.9	—
TF	6	12	38.3	0.42	8.88	45.4	37.6	99.8	83.6	227	83.6	201
LP	8	12	38.3	0.42	9.14	30.3	21.2	63.1	112	148	55.2	—
TF	8	12	38.3	0.42	8.88	32.1	22.5	66.8	118	148	58.5	162
LP	6	12	76.6	0.42	9.14	112	44.7	120	195	231	149	—
TF	6	12	76.6	0.42	8.88	118	47.4	127	206	240	158	—
LP	8	12	76.6	0.42	9.14	63.8	31	84	126	164	116	—
TF	8	12	76.6	0.42	8.88	67.5	32.8	88.9	134	161	123	—
LP	6	12	38.3	0.64	12	108	60.3	160	216	396	216	—
TF	6	12	38.3	0.64	10	132	74.1	197	265	379	265	—
LP	8	12	38.3	0.64	12	90.5	39.9	110	141	316	141	242
TF	8	12	38.3	0.64	10	111	48.9	135	173	261	173	—
LP	6	12	76.6	0.64	12	179	100	199	271	446	271	—
TF	6	12	76.6	0.64	10	219	123	244	333	487	333	—
LP	8	12	76.6	0.64	12	111	74.2	143	182	316	182	—
TF	8	12	76.6	0.64	10	136	91.1	175	223	359	223	—
BP	6	12	38.3	1.3	32	97	59	106	178	248	176	—
BP	8	12	38.3	1.3	32	64.1	43.2	75.8	135	180	121	234
BP	6	12	76.6	1.3	32	233	110	123	201	256	188	—
BP	8	12	76.6	1.3	32	136	81	91.1	153	180	139	—

TABLE VII
PREDICTED BREAKDOWN POWERS FOR THE EXPERIMENTAL VERIFICATION SET OF ESA ACTIVITY 2.

K	f_m (GHz)	Δf (MHz)	d (mm)	V (W)	20G (W)	20GB (W)	PM (W)	ES-N (W)	ES-F (W)	GNS (W)	MEAS (W)
3	11	99	0.4	35	11.2	7.7	16.1	21.5	25.8	21.5	—
3	11	198	0.4	35	57	11.6	17.9	22.8	26.8	22.8	—
4	11	198	0.4	35	19.4	8.8	12.8	16.9	19.7	16.9	37
3	11	396	0.4	35	50.1	19.6	19.6	23.8	26.8	23.8	63
5	11	198	0.4	35	10.3	6.9	9.9	13.4	15.8	13.4	—
10	11	99	0.4	35	2.6	1.8	3.8	5	7.9	5.5	10
3	11	99	0.7	34	127	32.9	57.3	88.6	88	88.6	92
3	11	198	0.7	34	165	61.4	61.9	94.1	90.6	94.1	128
4	11	198	0.7	34	95.9	45	44.9	68.9	72.7	68.9	80
3	11	396	0.7	34	165	61.4	66.2	94.5	92.7	94.5	—
5	11	198	0.7	34	69.6	36.4	35.5	53.3	58.1	53	65
10	11	99	0.7	34	12.9	9.3	15.2	26.9	29.1	21.5	20
3	11	99	2	37	1132	436	423	618	696	618	—
3	11	198	2	37	1132	436	441	623	696	623	—
4	11	198	2	37	624	324	326	491	581	491	—
3	11	396	2	37	1132	388	462	618	808	611	—
5	11	198	2	37	479	260	262	395	465	395	—
10	11	99	2	37	226	129	122	196	247	199	182

TABLE VIII
PREDICTED BREAKDOWN POWERS FOR THE EXPERIMENTAL VERIFICATION SET OF CNES AND THALES ALENIA SPACE ACTIVITY.

f_1 (GHz)	f_2 (GHz)	d (mm)	V (V)	20G (W)	20GB (W)	PM (W)	ES-N (W)	ES-F (W)	MEAS (W)
4.22	4.25	0.2	2.55	28.4	28.2	53.2	63.3	62.1	100
4.2175	4.2525	0.2	2.55	28.5	28.2	54.3	65.4	63.7	87
4.215	4.255	0.2	2.55	28.7	28.2	55.4	67.5	65.2	89
4.21	4.26	0.2	2.55	29	28.4	57.3	71.2	64.5	100
4.205	4.265	0.2	2.55	29.5	28.5	58.9	74.9	66	117
4.2	4.27	0.2	2.55	30.1	28.7	60.4	78	64.5	95
4.19	4.28	0.2	2.55	31.5	29.1	62.5	78	66.8	112
4.17	4.3	0.2	2.55	36	30.4	65.5	81.9	69.5	155
4.15	4.32	0.2	2.55	43.8	32.1	67.4	92.9	71.1	195
4.07	4.4	0.2	2.55	282	46	70.7	99.6	77.3	269
3.6	4.4	0.2	2.6	—	—	62.5	110	94.5	234
4.22	4.25	0.3	3.13	48.4	48	84.4	98.2	97.7	102
4.2175	4.2525	0.3	3.13	48.5	47.9	86.2	99.9	99.2	91
4.215	4.255	0.3	3.13	48.6	47.9	88	101	102	87
4.21	4.26	0.3	3.13	49	47.9	91.1	105	102	100
4.205	4.265	0.3	3.13	49.5	47.9	93.4	108	104	106
4.2	4.27	0.3	3.13	50.3	48	95.3	110	105	83
4.19	4.28	0.3	3.13	52.1	48.2	98.3	114	105	91
4.17	4.3	0.3	3.13	58.5	49.3	102	113	110	123
4.15	4.32	0.3	3.13	69.9	51.2	104	122	112	89
4.07	4.4	0.3	3.13	427	67.8	107	125	115	157
3.6	4.4	0.3	3.18	—	—	94.5	120	94.5	129

[11] S. Lin, H. Wang, Y. Li, C. Liu, N. Zhang, W. Cui, and A. Neuber, "Multipactor threshold calculation of coaxial transmission lines in microwave applications with nonstationary statistical theory," *Physics of Plasmas*, vol. 22, no. 8, p. 082114, 2015. [Online]. Available: https://doi.org/10.1063/1.4928421

[12] V. E. Semenov, E. I. Rakova, D. Anderson, M. Lisak, and J. Puech, "Multipactor in rectangular waveguides," *Physics of Plasmas*, vol. 14, no. 3, p. 033501, 2007. [Online]. Available: http://link.aip.org/link/?PHP/14/033501/1

[13] A. Perez, V. Boria, B. Gimeno, S. Anza, C. Vicente, and J. Gil, "Multipactor analysis in circular waveguides," *Journal of Electromagnetic Waves and Applications*, vol. 23, no. 11-12, pp. 1575–1583, 2009.

[14] C. Vicente, "Multipactor and corona discharge: Theoretical fundamentals and analysis with CST and Spark3D software tools," in *2017 IEEE International Symposium on Electromagnetic Compatibility Signal/Power Integrity (EMCSI)*, Aug. 2017, pp. 1–48.

[15] S. Anza, M. Mattes, C. Vicente, J. Gil, D. Raboso, V. E. Boria, and B. Gimeno, "Multipactor theory for multicarrier signals," *Physics of Plasmas*, vol. 18, no. 3, p. 032105, 2011. [Online]. Available: http://link.aip.org/link/?PHP/18/032105/1

[16] S. Anza, C. Vicente, J. Gil, M. Mattes, D. Wolk, U. Wochner, V. Boria, B. Gimeno, and D. Raboso, "Prediction of multipactor breakdown for multicarrier applications: The quasi-stationary method," *Microwave Theory and Techniques, IEEE Transactions on*, vol. 60, no. 7, pp. 2093 –2105, Jul. 2012.

[17] X. Wang, J. Shen, J. Wang, Q. Song, Z. Wang, Y. Li, R. Wang, T. Hu, Y. Xia, Q. Sun, X. Yin, W. Cui, H. Zhang, X. Zhang, C. Liu, C. Li, and L. Ran, "Monte carlo analysis of occurrence thresholds of multicarrier multipactors," *IEEE Transactions on Microwave Theory and Techniques*, vol. 65, no. 8, pp. 2734–2748, Aug 2017.

[18] *Space Engineering: Multipacting Design and Test*. ESA Publication Division, The Netherlands, May 2003, vol. ECSS-E-20-01A, edited by ESA-ESTEC.

[19] *Space Engineering: Multipactor Design and Test*. ESA Requirements and Standards Office, The Netherlands, June 2020, vol. ECSS-E-ST-20-01C, edited by ESA-ESTEC.

[20] S. Anza, C. Vicente, J. Gil, M. Mattes, D. Wolk, U. Wochner, V. Boria, B. Gimeno, and D. Raboso, "Multipactor prediction with multi-carrier signals: Experimental results and discussions on the 20-gap-crossing rule," in *Antennas and Propagation (EuCAP), 2014 8th European Conference on*, Apr. 2014, pp. 1638–1642.

[21] T. P. Graves, *Standard/Handbook for Radio Frequency (RF) Breakdown Prevention in Spacecraft Components*. Aerospace Corporation El Segundo CA, May 2014, vol. Report No. TOR-2014-02198.

[22] S. Anza, C. Vicente, B. Gimeno, V. E. Boria, and J. Armendariz, "Long-term multipactor discharge in multicarrier systems," *Physics of Plasmas*, vol. 14, no. 8, pp. 082 112–082 112–8, Aug. 2007.

[23] J.-C. Angevain, L. Drioli, P. Delgado, and C. Mangenot, "A boundary function for multicarrier multipaction analysis," in *Antennas and Propagation, 2009. EuCAP 2009. 3rd European Conference on*, Mar. 2009, pp. 2158 –2161.

[24] A. J. Marrison, R. May, J. D. Sanders, A. D. Dyne, A. D. Rawlins, and J. Petit, "A study of multipaction in multicarrier RF components," Culham, U.K., AEA Technology for ESTEC Ref. AEA/TYKB/31761/01/RP/05, Jan. 1997.

[25] S. Anza, C. Vicente, D. Raboso, J. Gil, B. Gimeno, and V. E. Boria, "Enhanced prediction of multipaction breakdown in passive waveguide components including space charge effects," in *IEEE International Microwave Symposium*, Atlanta, USA, Jun 2008, pp. 1095–1098.

[26] T. Sugai, Z. Shaw, J. Dickens, and A. Neuber, "Analysis of multipactor in a rectangular waveguide using Spark3D software," *Physics of Plasmas*, vol. 27, no. 11, p. 112108, 2020. [Online]. Available: https://doi.org/10.1063/5.0011641

[27] *Space Engineering: Multipactor Handbook*. ESA Requirements and Standards Office, The Netherlands, June 2020, vol. ECSS-E-HB-20-01A, edited by ESA-ESTEC.

[28] J. Rasch and J. F. Johansson, "Non-resonant multipactor - a statistical model," *Physics of Plasmas*, vol. 19, p. 123505, 2012.

[29] C. Vicente, M. Mattes, D. Wolk, H. L. Hartnagel, J. R. Mosig, and D. Raboso, "Multipactor breakdown prediction in rectangular waveguide based components," in *Microwave Symposium Digest, 2005 IEEE MTT-S International*, vol. 2, Long Beach, California, USA, edited by Institute of Electrical and Electronics Engineers. IEEE, New-York, Jun. 12-17 2005, pp. 1055–1058.

[30] S. Anza, "Multipactor in Multicarrier Systems. Theory and Prediction," Ph.D. dissertation, 2014.

[31] K. Price, R. M. Storn, and J. A. Lampinen, *Differential Evolution: A Practical Approach to Global Optimization*. Springer, 2005.

[32] J. Greenwood, "The correct and incorrect generation of a cosine distribution of scattered particles for Monte-Carlo modelling of vacuum systems," *Elseviewer Science, Vacuum*, vol. 67, no. 2, pp. 217–222, Sep. 2002.

[33] ECSS, "Multipactor Tool v1," *http://www.aurorasat.es/multipactortool.php*.

[34] S. Anza, C. Vicente, J. Gil, V. E. Boria, and D. Raboso, "Experimental verification of multipactor prediction methods in multicarrier systems," in *2016 46th European Microwave Conference (EuMC)*, Oct 2016, pp. 226–229.

Sergio Anza was born in Madrid, Spain, in 1978. He received the B.S. degree in telecommunications engineering in 2002 from the Universidad Politecnica de Valencia, Spain, and the M.S degree in aerospace science and technology in 2006 from the Universitat Politecnica de Catalunya, Barcelona, Spain. He received his Ph.D. in telecommunications engineering in 2014 from the Universidad Politecnica de Valencia, Spain.

From 2003 to 2006 he joined the Consejo Superior de Investigaciones Cientificas (CSIC), of the Spanish Ministry of Science. From 2007 to 2018, he worked with Aurora Software and Testing S.L. as R&D engineer. Since 2018, he is R&D Software Engineering Senior Manager at SIMULIA, a Dassault Systémes brand.

From 2015 to 2020, he has been member of the ECSS-E-ST-20-01 working group in charge of the update of the standard for multipactor design and test.

His current research interests include the areas of theory and numerical techniques for the modeling and prediction of non-linear phenomena in RF high power devices for space applications, with special emphasis on the study of the multipactor effect appearing in power microwave subsystems.

Jérôme Puech was born in 1974 in Rodez, France. He received the Engineering Diploma degree from the Telecom-SudParis (Institut National des Téléecommunications), Evry, France, in 1998.

In January 2000, he joined the Centre National d'Etudes Spatiales, Toulouse, France where he had been involved in microwave research activities mainly oriented toward microwave breakdown phenomena (Multipactor effect, Corona effect) within space components and traveling-wave tubes. Since February 2020, he has been working in the field of radiometric remote sensing in the Radar Instrument and performances department.

David Raboso, born in Alcazar de San Juan (Spain) in 1967, studied physics at the Autonomous University of Madrid. In 1992 he joined Payloads Systems Division of the European Space Agency (ESA) in the Netherlands where he became responsible for all activities related to RF breakdown in microwave space components. In 2002, he completed a Master degree in Space Engineering given by the University of Delft in the Netherlands and in 2018 he became telecommunications engineer ¨honoris causa¨ at the University Polytechnic of Valencia. His participation in space programs is extensive starting with pioneer observation satellites to modern interplanetary missions. Since 1994 he is chairman of the international conference covering issues of RF breakdown and passive intermodulation (Mulcopim) as well as ESA's responsible for updating the standards related to this discipline. Presently, he manages the joint ESA-VSC European laboratories in high power RF and space materials in Valencia.

Ulrich Wochner was born in Balingen, Baden–Württember, Germany, in 1968. He received the Diplom-Physicist degree from Eberhard Karls University Tübingen, Tübingen, Germany, in 1997. In 2001, he joined TESAT Spacecom GmbH&Co. KG, Backnang, Germany, as an RF Engineer with the Tesat Test Facility, where he was focused on highpower testing. Since 2004, he has been responsible for the RF-Components at the RF-Engineer Development Department, TESAT Spacecom GmbH&Co. KG.

Philippe Mader received the Ph.D. degree in applied mathematics from the Paul Sabatier University, Toulouse, France, in 2002.

He is currently RF engineer at Thales Alenia Space, Toulouse, France. Since 2003, he has been involved in power handling studies (Multipactor, PIM and Corona) for RF space components.

Olivier Koch received his Diploma in electrical Engineering from the RWTH Aachen University (Germany) in 2004. From 2004 till 2009 he worked as a research assistant at RWTH Aachen University. Since 2010 he is a payload system engineer at OHB System, Bremen, Germany. His research interests include (GNSS) payload performance and Multipactor.

Jean-Christophe Angevain was born in Montpellier, France, in 1971. In 1995, he received his engineering degree in telecommunications from Ecole Nationale Supérieure des Télécommunications de Bretagne, in Brest, France, and his MSc in Electronics and Electrical Engineering from University College London, United Kingdom. In 1997, he joined Alcatel Espace, (now Thales Alenia Space France, TAS-F), in Toulouse. He has held various positions of increasing responsibility in the Department of Spaceborne Antennas of Thales Alenia Space. As Antenna Product Manager, he was in charge of the procurement of the Cryosat 1 & 2 antennas for the Siral instrument. At this position, he was also responsible for the design and the development of the telecommunication antennas of Arabsat 4AR and the radiometer altimeter antenna of Altika instrument for the French-Indian SARAL satellite. In 2007, he joined the European Space Agency (ESA) as an Antenna Engineer in the Antenna and Sub-millimetre Wave Section in the Directorate of Technology, Engineering and Quality, in Noordwijk, the Netherlands. He was mainly in charge of several key R&Ds aiming at the development of a European large deployable reflector antenna. He provided support to several ESA telecommunication and Earth Observation projects such as Alphasat, EDRS, Sentinel 3, Sentinel 6, ROSE-L. He co-organized and chaired the 37th ESA antenna Workshop on large deployable antennas in 2016. He was member of the ECSS group in charge of the update of standard for multipactor design and test from 2015 to 2020. In 2020, he joined the Earth Observation Programmes (D/EOP) directorate in ESA, as Earth Observation microwave payload engineer. He has been working on radiometer and atmospheric radar instruments. He has been teacher of the European School of Antennas since 2008. He was co-recipient of the "Best Innovative Paper Prize" award of the 32nd ESA antenna workshop. He is also co-inventor of 2 patents.

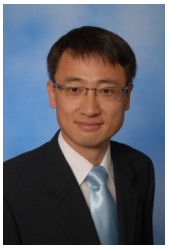

Un-Pyo Hong studied electrical engineering at Kyungpook National University in Daegu, South-Korea and earned B.S. in 1990. After graduation, he joined LG-Precision in South-Korea as research engineer (1993). Later, he came to Germany and studied electrical engineering at Ruhr-University in Bochum where he earned Diploma (Dipl. -Ing) in 2001. After completion of his degree, he joined Airbus Defence and Space (former Astrium) and developed a number of antenna feed systems for satellites and ground stations as RF engineer. Currently, he was a team member working for ECSS-E-ST-20-01C.

Per Magnusson, born 1971, studied Engineering Physics at Chalmers University of Technology from 1990 to 1996 and economics in combination with German language in 1993-1994. In 1996 he joined Saab Ericsson Space AB, now RUAG Space Sweden, where he is working as an antenna and communication systems engineer.

Isabel Montero is currently Research Professor of the Spanish National Research Council (CSIC), Spain. She is head of the Surface Nanostructuring for Space and Terrestrial Communications Group of the Materials Science Institute of Madrid (ICMM-CSIC). She is director of Spanish physics laboratory on secondary electron emission (SEY) of CSIC. She is expert in surface spectroscopic techniques and in low- secondary electron emission surfaces and coatings to avoid multipaction effect. She is a Working Group member of the ECSS Multipactor Working Group ECCS-E-ST-20-01-Multipaction, ASD-EUROSPACE.

Mohammed Belhaj was born in Tunis, in 1973. He received the Master degree in physics from the Joseph Fourier University, Grenoble France, Ph.D. degree in from the university de Reims, Reims, France in 2021. In 2021 he was a Post-Doctoral Research Fellow with the IXL labortory, Talence, France. In 2004, he was appointed as an Assistant Professor of applied physics, and joined the Department of physics, Institute of Applied Science and technology, Tunis, Tunisia. In 2008 he joined as researcher the ONERA-The French Aerospace Lab, Toulouse, France were he is currently working. His research interests include electron beam-solid interactions, secondary electron, charging of dielectrics under radiations, multipactor effect.

John Petit received his BSc degree in physics from Sussex University in 1980. Since then he has worked for a range of companies & institutions, covering the areas of defence, research, mobile systems and space technology, which has included working at Marconi, University of Kent at Canterbury, COM DEV (UK), Honeywell and ESTEC (Netherlands). His current position as senior researcher is with Val Space Consortium, based in Valencia, Spain, where he is responsible for overseeing a 3 year project funded by ESA, investigating Multipactor prediction techniques in relation to GNSS signals. His principle experience is in the field of high power discharge effects such as multipactor and gas breakdown in space components.

Jordi Gil received the Licenciado degree in physics from the Universidad de Valencia, Spain, in 2000, and the Ph.D. degree in telecommunications engineering from the Universidad Politécnica de Valencia, Spain, in 2010.

From 2001 to 2004, he was Researcher with the Aeronautical Italian Company, Ingegneria Dei Sistemi-S.p.A., under the frame of the V European Framework Programme. From 2004 to 2006, he joined the Microwave Applications Group, Universidad Politécnica de Valencia, under the frame of a European reintegration grant funded by the VI European Framework Programme. In 2006, he cofounded the company Aurora Software and Testing SL, devoted to the space sector, where he combined his research activities with the Managing Director role. Since 2017, the company became part of Dassault Systèmes SE. (SIMULIA Brand), where he is currently Technology Manager. His current research interests include numerical methods in computer-aided techniques for electromagnetic analysis and design of microwave passive components based on waveguide technology.

He was awarded in 2011 with the PhD Thesis Extraordinary Award at the Universidad Politécnica de Valencia.

Carlos Vicente (M'08) received the Diploma degree in physics from the Universidad de Valencia, Valencia, Spain, in 1999. He received his Ph.D. in telecommunications engineering in 2005 from the Technical University of Darmstadt, Germany. In his doctoral thesis, Dr. Vicente researched high power effects in communications satellites such as RF breakdown and passive intermodulation. In 2006, he co-founded the company Aurora Software and Testing S. L. (Aurorasat). Dr. Carlos Vicente currently serves as SIMULIA Electromagnetics Industry Process Senior Manager for SIMULIA, a Dassault Systémes brand.

Vicente E. Boria (S'91-A'99-SM'02-F'18) was born in Valencia, Spain, on May 18, 1970. He received his "Ingeniero de Telecomunicación" degree (with first-class honors) and the "Doctor Ingeniero de Telecomunicación" degree from the Universidad Politécnica de Valencia, Valencia, Spain, in 1993 and 1997, respectively. In 1993 he joined the "Departamento de Comunicaciones", Universidad Politécnica de Valencia, where he has been Full Professor since 2003. In 1995 and 1996, he was holding a Spanish Trainee position with the European Space Research and Technology Centre, European Space Agency (ESTEC-ESA), Noordwijk, The Netherlands, where he was involved in the area of EM analysis and design of passive waveguide devices. He has authored or co-authored 15 chapters in technical textbooks, 200 papers in refereed international technical journals, and over 250 papers in international conference proceedings. His current research interests are focused on the analysis and automated design of passive components (in particular filters and multiplexers) in several technologies, as well as on the simulation and measurement of power effects in high-frequency devices and systems. Dr. Boria has been a member of the IEEE Microwave Theory and Techniques Society (IEEE MTT-S) and the IEEE Antennas and Propagation Society (IEEE AP-S) since 1992. He is also member of the European Microwave Association (EuMA), and has been the Chair of the 48th European Microwave Conference held in Madrid, Spain. He acts as a regular reviewer of the most relevant IEEE and IET technical journals on his areas of interest. He has been Associate Editor of IEEE Microwave and Wireless Components Letters (2013-2018) and IET Electronics Letters (2015-2018). Presently, he serves as Subject Editor (Microwaves) of IET Electronics Letters, and as Editorial Board member of International Journal of RF and Microwave Computer-Aided Engineering. He is also member of the Technical Committees of the IEEE-MTT International Microwave Symposium and of the European Microwave Conference.